Engineering Structures 318 (2024) 118757

Contents lists available at ScienceDirect

Engineering Structures

journal homepage: www.elsevier.com/locate/engstruct

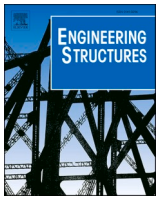

Prediction of axial-compressive behaviour of bare cold-formed steel studs through a new stud-to-track contact modeling approach

Sohini Mishra *, Daniel P. McCrum

Modern Methods of Construction Research Group, School of Civil Engineering, Newstead Building, University College Dublin, Dublin 4, Ireland

ARTICLE INFO

Keywords:
Finite element analysis
Cold-formed steel studs
Stud-to-track gap
Softened contact
Axial-stiffness
Contact-stiffness

ABSTRACT

This paper presents a new and accurate finite element contact-modeling approach, to predict the axial compressive behaviour of bare cold-formed steel (CFS) lipped-channel sections (studs) set in tracks under concentric, static axial compressive loading. Detailed finite element analysis (FEA) models of the stud-track assemblies are developed using the ABAQUS software. The new modeling approach is validated against test results and captures stud-to-track gap and contact normal behaviour, which significantly influences studs' axial compressive performance. Hard contact (HC) has been used widely in literature for its simplicity, although it overestimates axial structural stiffness. Two softened pressure-overclosure relationships, with linear (LSC) and piecewise linear (PLSC) functions, were investigated for the first time in axially loaded bare CFS studs. PLSC best-replicated studs' axial-compressive behaviour, post-peak response, and failure mechanism under track boundary conditions. PLSC slightly overestimated the axial stiffness by 1 %, underestimating axial shortening and ultimate capacity by 3 % and 6 %, respectively. HC significantly overestimated the axial stiffness by a factor of 3, with a 5 % overestimation of ultimate capacity. LSC failed to predict the accurate failure mechanism for studs having gauge thicknesses less than 3 mm. PLSC scale factors were established and were found to be closely correlated with studs' non-dimensional slenderness (λ), following bilinear relationships. New predictive equations were developed to determine the PLSC scale factors for λ ranging between 0.49 and 1.2 to enable designers to use accurately calibrated models to capture bare studs' complex axial compressive behaviour in the elastic and inelastic range.

1. Introduction

Cold-formed steel (CFS) load-bearing stud wall panels are becoming increasingly popular in the built environment, especially in low and medium-rise residential, commercial, and industrial sectors, due to their advantages over hot-rolled steel, such as improved construction speed, a higher strength-to-weight ratio, higher recycling rate, and reduced carbon emission [1,2]. However, the behaviour of CFS panelised structures is complicated due to the thin-walled cross-sections of CFS, which cause local, distortional, and global buckling modes. Such unique behaviour of CFS sections requires advances in numerical analysis and modeling techniques [3]. Case studies highlighting the complex features of load-bearing CFS panelised buildings, their advantages, and disadvantages at different phases of design and construction, e.g., architectural design, structural design, concept design durability, etc., have been reported in the literature by Dubina et al., [4], The Steel Construction Institute publications [5,6], and AISI reports [7]. Due to a lack of design guidance and numerical modeling techniques that exist particularly to account for vertical and gravity loading [8,9] in CFS load-bearing panels, practicing engineers consider CFS buildings only for low-rise solutions up to six or eight stories [4]. Kyvelou et al. [9] highlighted that, at present, the design of individual CFS structural components acting as the key load-bearing elements in CFS buildings is restricted to ideal conditions. To enable a more efficient design, actual conditions of load introduction and the restraint arising from practical situations or boundary conditions must be recognized. Conducting full-scale testing to address this issue is expensive and time-consuming. Therefore, as an alternative solution, there is a pressing need to develop accurate numerical modeling techniques that can precisely simulate real-world physical boundary and loading conditions. The significance of the current research lies in addressing these particular issues in the context of accurately numerically simulating the axial-compressive behavior of bare CFS studs set in tracks (which is a real-world boundary condition for studs employed in load-bearing CFS panelised buildings) through a

* Corresponding author.
E-mail addresses: sohini.mishra@ucdconnect.ie, sohiniucd@gmail.com (S. Mishra).

https://doi.org/10.1016/j.engstruct.2024.118757
Received 11 May 2024; Received in revised form 20 July 2024; Accepted 6 August 2024
Available online 10 August 2024

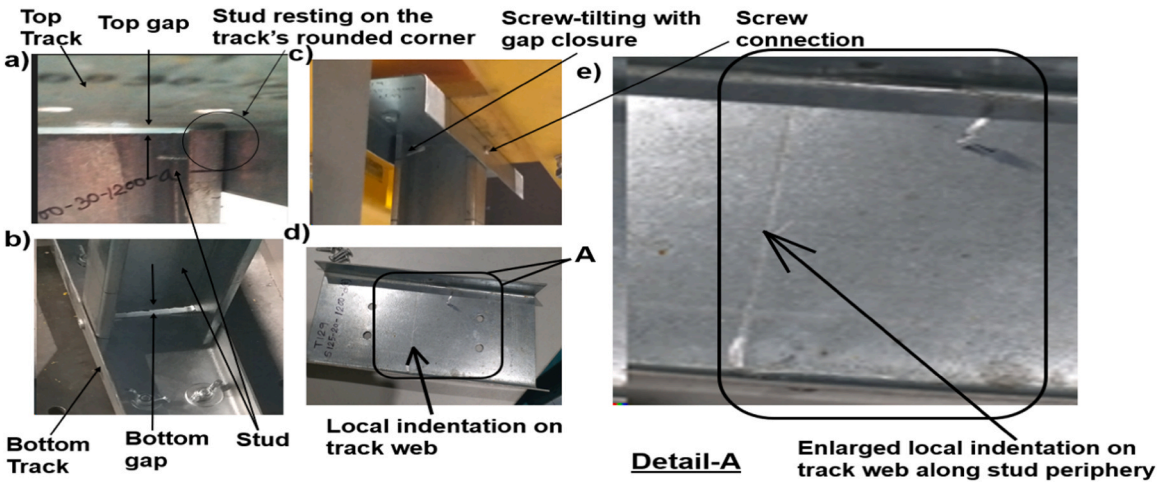

Fig. 1. a) & b) Stud-to-track gap at top and bottom, respectively, c) connection failure with gap closure, d) local indentation of the track-web, e) Detail-A, showing enlarged local indentation on track web after removal of stud.

new stud-to-track contact modeling approach. Studs are the primary gravity load-bearing components, predominantly subjected to axial compression in CFS wall panels [4,10,11], placed between the top and bottom tracks (header and footer), and connected with self-tapping screws. A gap exists between the stud and the track web as the stud initially makes contact with the track's rounded corner radius, not the web's flat portion [12,13]. The combined effect of the stud-to-track gap, tracks' warping rigidity, and nonlinear connection stiffness make the studs' boundary condition semirigid [13]. Due to this semirigid boundary condition, the behaviour of studs in the CFS stud wall panel is somewhere between a column (with full moment-fixity at the ends as in moment resisting frames) and a strut (with ideal pinned boundary condition having zero moment fixity at the ends) [13]. The general practice is to design the studs in CFS wall panels under axial compressive loading, following an 'all-steel' design, neglecting the beneficial effect of sheathing, which is also supported by Eurocode 3 [14]. Lawson et al. [15] mentioned that the contribution of sheathing strength to the axial load capacity of the bare CFS studs should not be overly relied upon because sheathing may be damaged or replaced at some stage. Moreover, Vieira et al. [16] have experimentally demonstrated that sheathing does not influence the studs' axial stiffness; it only influences their ultimate capacity and limit states. The 'all-steel' design approach considers the studs' boundary condition as pinned due to a lack of design guidance and numerical modeling guidance to assess the precise effect of the track boundary condition on the studs' axial compressive performance. Test data investigating the axial-compressive behaviour of bare CFS studs rarely exists in the literature. Ye et al. [17] and others [15,18,19] employed a single bare stud-track assembly as a comparator while experimentally investigating the axial-compressive behaviour of sheathed stud-wall panels with a constant cross-section of the stud-track assembly and varying sheathing types. The aforementioned studies did not explicitly report the load-axial shortening response of individual bare studs. Mishra et al. [13] recognized that no previous research investigated bare CFS studs' ultimate axial compressive strength, stiffness, load-deformation response, and failure mechanism along the entire load equilibrium path whilst considering the combined effect of the tracks' warping rigidity, nonlinear connection performance, stud-to-track gap, and the studs' various cross-sectional slenderness, under real-world track boundary conditions. Only LaBoube and Findlay [12] investigated the stud-to-track gap, amongst other parameters, for sheathed CFS stud wall panels to investigate the effect of the gap, particularly on the stud-to-track connection strength and the aesthetics of the sheathing. Vieira et al. [16] eliminated the stud-to-track gap to the maximum extent possible while investigating the axial compressive strength of sheathed stud wall panels. However, they [16] acknowledged that eliminating the stud-to-track gap did not replicate the 'real-life' stud-to-track connecting arrangement. To address this research gap, Mishra et al. [13] conducted comprehensive axial compressive load tests on forty-two industry-standard bare CFS studs having various web-slendernesses with the semirigid track boundary condition along with considering explicitly the effect of stud-to-track gap and nonlinear connection performance on bare CFS studs' axial compressive behaviour.The authors [13] demonstrated that the studs' axial compressive behaviour and the failure mechanism are significantly influenced by the track boundary condition compared to an ideal pinned boundary condition. The detailed structural mechanical failure mechanism of each bare CFS stud cross-section type and height under the track boundary condition and axial-compressive loading, is presented in the experimental paper by Mishra et al. [13]. Fig. 1 & Fig. 2 show the various features of the semirigid track boundary condition and their influence on the studs' axial compressive behaviour, as observed in the reference testing program by Mishra et al. [13]. As shown in Fig. 2, the studs exhibited a two-phased axial stiffness during the stud-to-track gap closure (loading Phase I in Fig. 1a & b) and post-gap closure until the peak load (loading Phase II in Fig. 1c). The tracks' warping rigidity caused the studs to experience higher axial compressive capacity than that in comparative tests with pinned boundary conditions. Moreover, with track boundary condition, the studs' Phase II axial stiffness was 30 % lower than that in the comparative test with pinned boundary conditions, indicating new modeling approaches are needed to capture this behaviour. After the test's completion, local indentation was observed on the track web along the stud periphery locations for all the studs (Fig. 1d and e). For the first time, this paper will develop an approach to accurately capture the studs' complex axial compressive behavior with

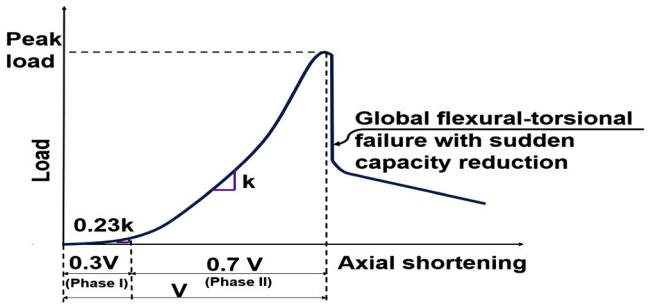

Fig. 2. Schematic of the studs' load-axial shortening response under concentric static axial compressive loading with a track boundary condition.

Table 1
Measured out-to-out cross-sectional dimensions, initial eccentricity, stud-to-track gap, and geometric imperfection.

Test No/ Specimen ID	Overall depth, h (mm)	Upper flange width, b1 (mm)	Lower flange width, b2 (mm)	Upper lip depth, c1 (mm)	Lower lip depth, c2 (mm)	Inner corner radius, r (mm)	Galvan-ized thickness, t (mm)	Measured Initial eccentricity $e_{0,\ end}$ (mm)	Measured stud-to-track gap (mm)		Measured geometric imperfections		
									Top	Bot	Local d_1/t	Distortional d_2/t	Twist d_φ *(deg)*
1/S75 −1.2 −1200 −1	73.9	42.4	42.2	8.1	8.2	1.8	1.2	−1.96	2.9	1.1	0.43	0.81	2.6
2/S75 −1.2 −1200 −2	73.9	42.8	42.5	8.3	8.0	1.8	1.2	-	2.8	0.98	0.23	1.21	2.7
3/S75 −1.2 −1200 −3	74.0	42.4	42.7	8.1	8.4	1.8	1.2	-	2.5	1.24	0.24	0.69	1.9
4/S75 −1.2 −1500 −1	73.9	42.3	42.9	8.7	7.5	1.8	1.2	−2.39	2.3	2.2	0.20	0.58	3.6
5/S75 −1.2 −1500 −2	73.8	41.7	42.8	8.7	7.5	1.8	1.2	-	4.1	4.0	0.22	0.31	4.6
6/S75 −1.2 −1500 −3	73.9	42.9	42.5	8.1	8.5	1.8	1.2	-	3.8	3.6	0.33	0.35	3.8
7/S75 −1.5 −1200 −1	75.7	42.3	42.9	8.1	8.5	2.2	1.5	0.72	1.9	2.9	0.40	0.68	1.8
8/S75 −1.5 −1200 −2	75.7	42.6	43.1	8.4	8.2	2.2	1.5	-	1.4	1.8	0.20	0.05	2.7
9/S75 −1.5 −1200 −3	#	#	#	#	#	#	#	#	#	#	#	#	#
10/S75 −1.5 −1500 −1	75.7	42.6	43.0	8.4	8.2	2.2	1.5	1.82	3.4	3.2	0.10	0.27	1.9
11/S75 −1.5 −1500 −2	75.8	42.8	43.1	8.7	7.7	2.2	1.5	-	3.7	3.1	0.20	1.2	3.5
12/S75 −1.5 −1500 −3	#	#	#	#	#	#	#	#	#	#	#	#	#
13/ S100 −1.2 −1200 −1	101.6	49.6	50.0	9.6	10.1	1.7	1.2	−0.73	1.0	2.0	0.43	0.52	2.9
14/ S100 −1.2 −1200 −2	101.5	49.5	50.2	9.5	9.8	1.6	1.2	-	4.8	3.1	0.45	0.51	2.7
15/ S100 −1.2 −1200 −3	#	#	#	#	#	#	#	#	#	#	#	#	#
16/ S100 −1.2 −1500 −1	102.0	49.8	50.1	10.0	9.2	1.7	1.2	0.88	1.4	1.3	0.43	2.29	2.3
17/ S100 −1.2 −1500 −2	101.9	49.7	49.9	9.6	9.9	1.6	1.2	-	1.3	1.4	0.58	1.93	2.8
18/ S100 −1.2 −1500 −3	102.0	50.0	50.3	9.9	9.7	1.7	1.2	-	3.1	3	0.09	2.36	2.5
19/ S100 −2.0 −1200 −1	99.5	51.4	50.8	12.8	13.4	3.2	2.0	−1.38	1.2	1.3	0.97	0.76	1.5
20/ S100 −2.0 −1200 −2	98.9	49.5	52.5	14.4	11.0	3.1	2.0	-	2.9	3.1	0.98	0.58	1
21/ S100 −2.0 −1200 −3	99.5	51.9	49.5	11.6	13.5	3.1	2.0	-	2.4	2.2	0.46	0.61	1.5
22/ S100 −2.0 −1500 −1	99.5	51.6	50.0	13.0	12.3	3.2	2.0	−1.23	2.4	1.9	0.10	0.707	1.2
23/ S100 −2.0 −1500 −2	99.4	50.0	52.8	11.9	13.5	3.2	2.0	-	2.8	2.7	0.71	0.56	0.8
24/ S100 −2.0 −1500 −3	99.4	52.7	49.7	12.1	13.4	3.2	2.0	-	4.2	1.8	0.20	0.82	0.8
25/ S100 −3.0 −1200 −1	100.3	50.0	51.4	19.3	17.4	4.3	3.1	−1.55	1.4	4.5	0.17	0.51	1.3
26/ S100 −3.0 −1200 −2	100.2	51.3	50.7	20.0	16.9	4.3	3.0	-	0.6	1.5	0.09	0.37	1.5
27/ S100 −3.0 −1200 −3	100.2	50.0	51.1	17.3	19.5	4.3	3.0	-	2.0	1.8	0.42	0.2	1.8
28/ S100 −3.0 −1500 −1	100.3	51.1	50.5	20.0	16.5	4.3	3.0	2.18	1.7	1.5	0.03	0.14	1.8
29/ S100 −3.0 −1500 −2	100.6	49.5	51.7	18.4	18.5	4.3	3.0	-	5.3	2.8	0.03	0.18	1.1
30/ S100 −3.0 −1500 −3	100.3	50.4	51.2	20.6	16.1	4.3	3.0	-	1.4	1.8	0.02	0.07	2.1

(*continued on next page*)

Table 1 (*continued*)

Test No/ Specimen ID	Overall depth, h (mm)	Upper flange width, b1 (mm)	Lower flange width, b2 (mm)	Upper lip depth, c1 (mm)	Lower lip depth, c2 (mm)	Inner corner radius, r (mm)	Galvan-ized thickness, t (mm)	Measured Initial eccentricity $e_{0,\ end}$ (mm)	Measured stud-to-track gap (mm)		Measured geometric imperfections		
									Top	Bot	Local d_1/t	Distortional d_2/t	Twist d_φ *(deg)*
31/ S125 −1.3 −1200 −1	124.5	52.4	51.8	22.0	16.7	2.3	1.2	−0.18	0.2	0.5	0.98	1.1	0.9
32/ S125 −1.3 −1200 −2	124.7	52.4	51.9	20.6	18.2	2.3	1.2	-	0.3	0.7	0.25	1.8	0.4
33/ S125 −1.3 −1200 −3	124.5	51.3	53.1	20.1	18.4	2.3	1.2	-	0.3	0.2	0.70	1.5	0.7
34/ S125 −1.3 −1500 −1	124.4	51.8	52.2	22.1	16.7	2.3	1.2	−1.5	0.9	0.96	0.59	1.14	0.9
35/ S125 −1.3 −1500 −2	124.7	53.1	51.6	18.1	20.3	2.3	1.2	-	0.8	0.7	0.90	1.8	1.6
36/ S125 −1.3 −1500 −3	124.5	52.0	52.8	17.8	20.4	2.3	1.2	-	0.2	0.5	0.39	1.4	1.2
37/ S125 −2.0 −1200 −1	125.1	51.5	52.0	17.1	19.2	3.2	2.0	2.25	1.2	1.9	0.98	1.1	2.9
38/ S125 −2.0 −1200 −2	125.2	52.3	51.2	18.2	18.2	3.2	2.0	-	3.9	2.3	0.36	0.58	1.8
39/ S125 −2.0 −1200 −3	125.3	52.7	52.2	18.0	17.8	3.2	2.0	-	2.5	3.9	0.30	0.68	2
40/ S125 −2.0 −1500 −1	125.2	51.4	52.1	19.1	17.7	3.2	2.0	−0.56	2.2	1.9	0.10	0.71	1.9
41/ S125 −2.0 −1500 −2	125.3	51.6	51.9	17.8	18.9	3.2	2.0	-	2.5	1.3	0.36	0.58	1.7
42/ S125 −2.0 −1500 −3	125.2	51.4	52.3	19.5	17.0	3.2	2.0	-	1.0	1.9	0.50	0.69	2.1

#The test data corrupted for test no 9,12&15 due to power disruption in the lab

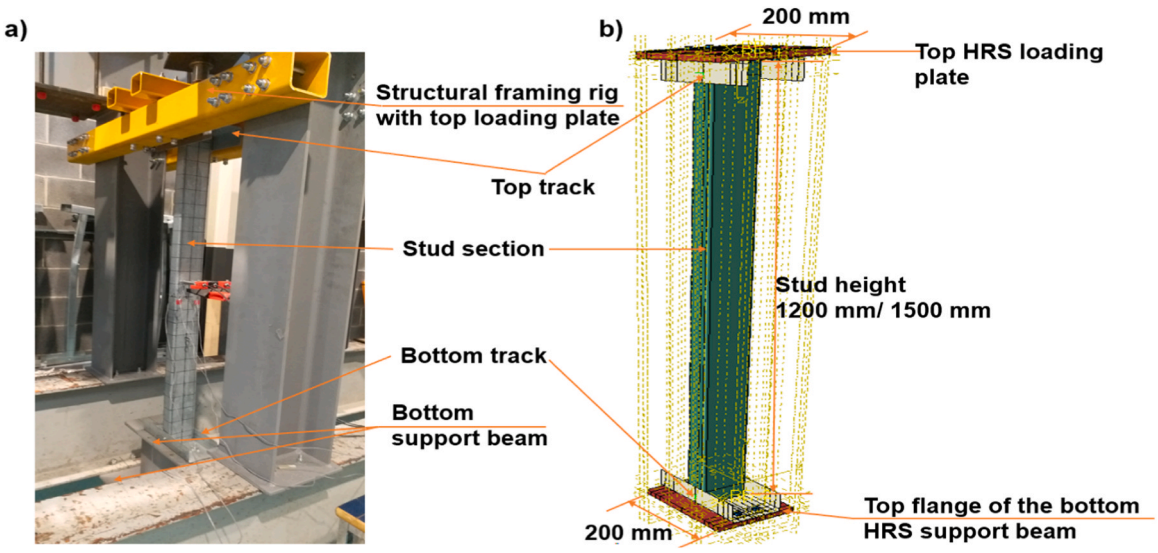

Fig. 3. a) Photograph of test setup; and b) elevation of FEA model.

the track boundary condition, as shown in Fig. 2, utilizing the extensive experimental database on the axial-compressive performance of bare CFS studs reported by Mishra et al. [13]. FEA modeling techniques have been developed to predict CFS studs' bare and sheathed ultimate strength and load-deformation responses under fire exposure with track boundary conditions [22,23]. Still, they did not accurately capture the effect of the restraint stiffness of the end tracks on the studs' performance, which is particularly important under compressive and lateral loading scenarios. Most modeling approaches using a track boundary condition in CFS panelised construction have focused on investigating the performance of sheathed and bare panels under lateral (seismic) loading rather than vertical loading [10,20]. Peiris and Mahendran [22] applied a MPC beam constraint between the stud and track in the FEA model.

However, Kechidi et al. [8] and Kyvelou et al. [9] recognized that such modeling techniques with tie constraints assume that the stud fully bears on the track initially, whereas, in reality, a gap always exists between the stud and track, making the studs' initial load-axial shortening response nonlinear. Another technique to model the accurate interaction between the stud and tracks in CFS wall panels is modeling the stud-to-track contact interaction. In this method, during global analysis, the tangential and normal contact behaviour was assigned between interconnected parts of the stud-wall panel, e.g., stud-to-track [21], noggings to studs, track-to-top, and bottom support plates, etc. [10,20, 22] The tangential or frictional behaviour was simulated using Coulomb's friction coefficient. In the local normal direction (perpendicular to the contact surface), hard contact (HC) has been employed so that the connecting parts do not penetrate each other numerically. However, this is not the case, as shown in Fig. 1d & e; indentation on the track web around the stud-periphery exists after the stud bares on the track web. Furthermore, Niari et al. [20] recognized that existing numerical models investigating stud-wall panels' performance under seismic/lateral loading overestimated the stud-wall panels' ultimate structural strength and lateral structural stiffness with HC compared to respective test data. More recently, a linear softened pressure-overclosure relationship [23] along the direction normal to the contact surface was adopted by [24–26] to successfully replicate the web-crippling behaviour of simply supported CFS beams. However, the softened contact parameters would vary with the variation of structural component types and boundary conditions. No previous research has implemented softened contact interaction to study CFS studs' behaviour with the track-boundary conditions under axial-compressive loading.'.

This research proposes a new numerical FEA contact modeling approach validated by testing that can be employed to accurately predict the individual bare CFS studs' axial compressive strength and stiffness behaviour along with the complex buckling mode interactions, failure mechanism, and post-peak response under semirigid track-boundary conditions. The HC and two different softened pressure overclosure relationships with a linear function (LSC), as well as a piecewise linear function (PLSC) [23], are studied and compared with test data. Finally, new predictive relationships between the studs' nondimensional slenderness ratios (λ) and the softened contact scale factors are proposed to provide designers with accurately calibrated FEA models to capture bare studs' complex axial behaviour in the elastic and inelastic ranges.

2. Descriptions of the reference experimental program

Forty-two industry-standard lipped channel sections (used as studs) of five different thicknesses (1.2–3 mm) and three depths (75,100 and 125 mm) were tested with track boundary conditions (refer to [13] for more details). The studs were connected to a small (300) mm length track at the top and bottom with industry-standard No 12 self-tapping (S/T) screws. For the measured average out-to-out dimensions of the tested studs, corresponding tracks, and the tensile coupon test properties for five different gauge thicknesses of the tested specimens, refer to [13]. The measured parameters, e.g., initial eccentricity at the sample end, $e_{0,end}$, the stud-to-track gap, geometric imperfections, and out-to-out cross-sectional dimensions for each stud sample, are presented in Table 1. An initial eccentricity towards the web is considered positive. The local and distortional imperfections are normalized with respect to base metal thickness, t, and denoted as d1/t & d2/t, respectively. In Table 1, the Specimen ID provides details about the specimen, e.g., S125–2.0-1200–1; S is the stud; 125 is the specimen's overall depth in mm; 2.0 is the thickness in mm (including galvanizing); 1200 is the stud height in mm, and 1/2/3 represents the number of repeat tests(i.e., S125–2.0-1200–1, meaning the first sample for the S125–2.0-1200 stud).

3. Numerical investigation

Fig. 3 shows the test setup photograph and the stud-track assembly's corresponding elevation with the track-boundary conditions developed in the FEA model using ABAQUS v.6.14 [23].

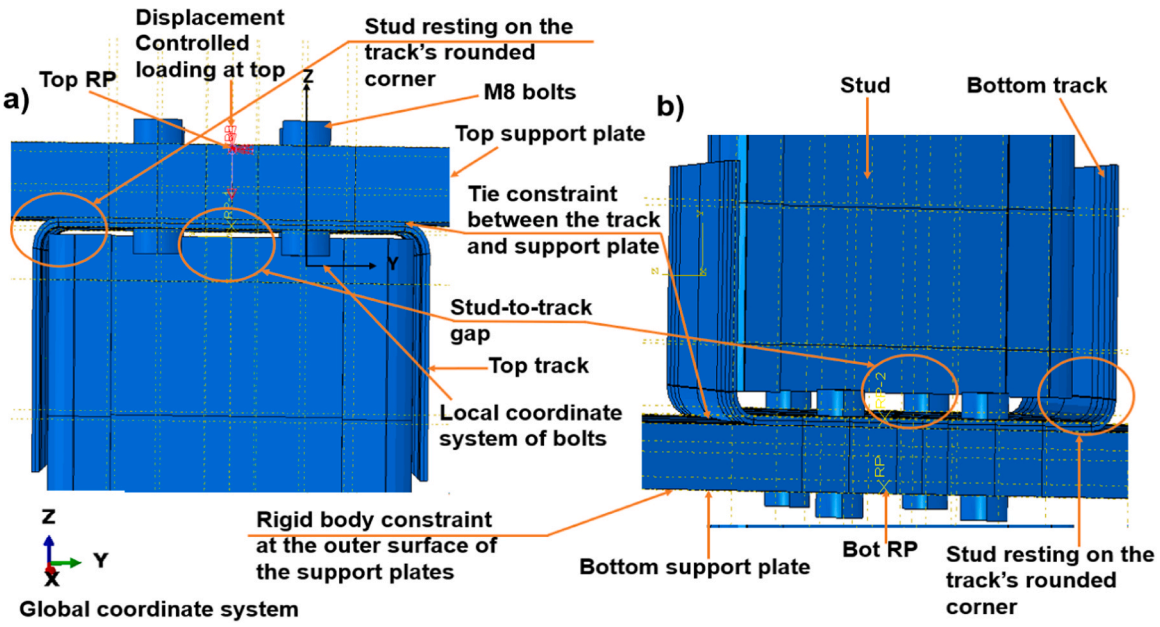

Fig. 4. Elevation view of the track-boundary condition with measured stud-to-track-gap in the FEA model a) top and b) bottom.

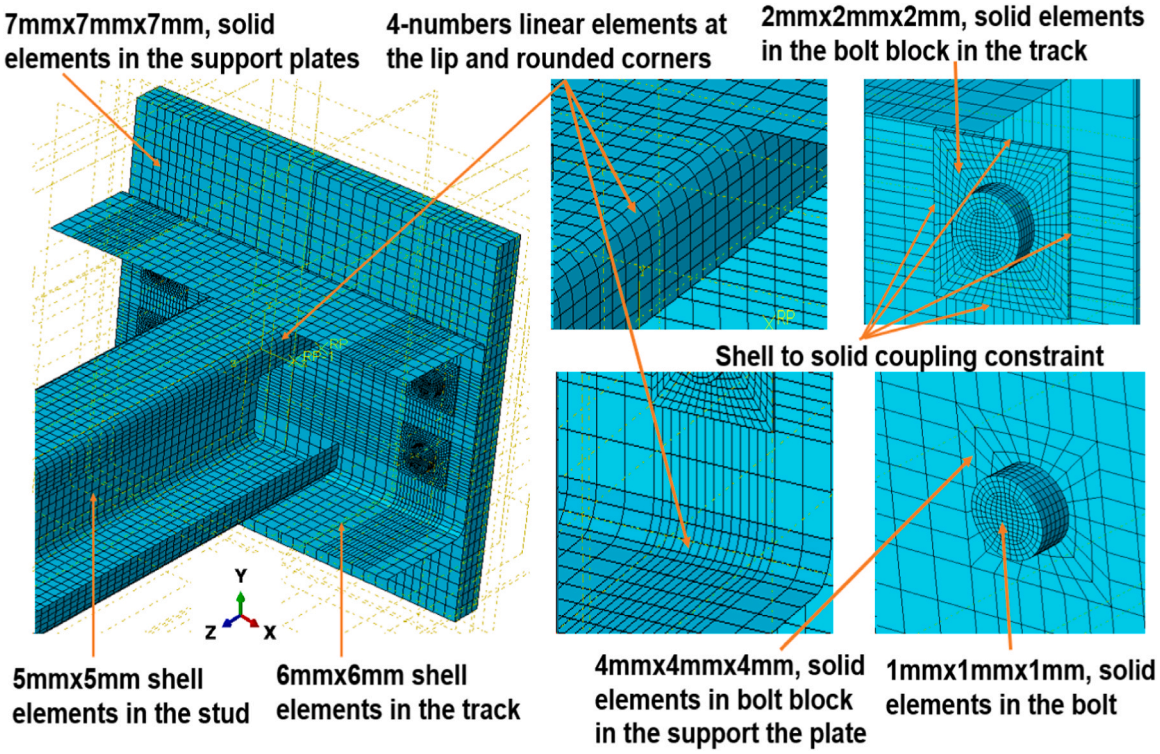

Fig. 5. Meshing technique and element type used in the FEA model.

3.1. The overall geometrical arrangement, including the stud-to-track gap, support plates, and end restraints

Fig. 4 details the overall geometrical arrangement of the track boundary conditions in the FEA model and the global coordinate system. The measured stud-to-track gap (refer to Table 1) was explicitly modeled at the top and bottom for every stud as per the test setup [13], with all hot rolled steel (HRS) support steel modeled. The M8 bolts connecting the tracks to the support plates in a 10 mm dia bolt hole, were modeled with an 8 mm diameter bolt-shank and 13 mm diameter x 5.5 mm thick bolt-head. Reference points denoted as TopRP and BotRP were created at the outer surface of the top (loading plate [13]) and bottom support plates (modeled as the top flange of the bottom support beam [13]), respectively, at the intersection point of the measured initial eccentricity and center of gravity (CG) of the support plates. A rigid body constraint was applied between the Top RP, BotRP, and the support plate's outer surface to ensure uniform distribution of applied loading. A tie constraint was applied between the track webs and the support plates' inner surfaces. Bot RP was fully constrained, and Top RP was fully constrained except for axial displacement along the global z-axis

Table 2
Results of mesh sensitivity study.

The mesh size of the stud (mm x mm)	Tested peak load (kN)	FEA peak load (kN)	CPU time (Sec)	Percentage difference in analytical peak load compared to tested peak load (%)	Percentage difference in CPU time compared to CPU time with 5 × 5 mm mesh size (%)
10 × 10	118.7	118.00	4.7	0.59	−20.34
8 × 8	118.7	116.60	4.6	1.80	−22.03
5 × 5	118.7	112.80	5.9	4.96	-
2 × 2	118.7	112.60	10.6	5.21	79.66

(vertical). The stud-to-track screwed connections (Fig. 1b and c) were modeled with discrete fastener features used to couple multiple surfaces, as was also followed by [10,22]. The radius of the connector was assigned as the physical radius of 2.75 mm of the S/T screws used in the testing program [13]. The fasteners were assigned connector properties to describe the relative motion between the stud and track. Each connector's strength and stiffness properties were specified using Pham and Moen's proposed equations [27].

3.2. Element type and mesh size

Fig. 5 shows the meshing technique adopted in this study. The 4-noded linear shell element with reduced integration, S4R, was used to model the stud and tracks, as adopted in previous research [8,20,28], since it is suitable for thin-walled CFS members with large strain analysis and geometrically nonlinear problems. The support plates and bolts were modeled with an 8-noded linear brick (solid) element, C3D8R, with reduced integration. An accurate numerical modeling technique [29] that combines a shell (S4R) and a small number of solid (C3D8R) elements was employed to model the bolt holes surrounding areas (bolt block in Fig. 5). A mesh sensitivity study was conducted on a benchmark stud sample S100–2.0-1500–3, using four different square mesh sizes of the studs: 10 mm x 10 mm, 8 mm × 8 mm, 5 mm × 5 mm, and 2 mm × 2 mm. The results of the mesh sensitivity study are reported in Table 2, where it can be observed that the mesh density significantly impacted the predicted peak load, as was also reported by [30]. The coarser mesh sizes, 10 mm square and 8 mm square, yielded an average of 1.2 % lower axial compressive capacity than the tested peak capacity. However, the crude mesh sizes (10 mm square and 8 mm square) caused significant inertia effects, resulting in high noise in the load-axial shortening response; hence unreliable results. The 5 mm square mesh predicted a peak load closer to the tested peak load with a 5 % underestimation and negligible noise in the load-axial shortening response. The computational time needed by the 10 mm square and 8 mm square mesh were similar while being 21 % higher than the CPU time needed for the 5 mm square mesh. Using the 2 mm square mesh sizes was computationally demanding, with an 80 % higher computational time than the 5 mm square mesh and negligible gain in the accuracy of the result. Based on the mesh sensitivity study, a mesh size of 5 mm × 5 mm for the studs was adopted to balance the computational time and accuracy. Four numbers of S4R shell elements were employed at the rounded corner of the studs and tracks and the studs' lip to accurately replicate the distortional buckling phenomena and ensure proper load transfer between the web and flange [19]. The mesh sizes adopted for the tracks, bolts, and support plates were 6 mm × 6 mm, 1 mm × 1 mm x 1 mm, and 7 mm × 7 mm x 7 mm, respectively, having little effect on the peak predicted load. A finer mesh size was adopted for the bolt blocks to achieve computational accuracies [29]: 2 mm × 2 mm x 2 mm on tracks and 4 mm × 4 mm x 4 mm on support plates.

3.3. Material model

Gardener [31] and Walport et al. [32] acknowledged that CFS's nonlinear material stress-strain response directly influences the structural behaviour at the cross-section, member, and frame levels. The accurate consideration of the material nonlinearity causes greater structural deformations resulting from the loss of material stiffness. Hence, Gardener [31] recommended that to predict the accurate internal forces, deformations, and structural stiffness, the rounded stress-strain behaviour of CFS must be included in the material model during the structural numerical analysis. This research adopted a modified two-stage Ramberg-Osgood [33] model developed and recommended by Gardner and Yun [34] to accurately describe the stress-strain behaviour of CFS, including its' rounded corner. The predictive expressions for describing the stress-strain behaviour of CFS, as per [34], are summarised below. [34].

$$\epsilon = \begin{cases} \dfrac{f}{E} + 0.002\left(\dfrac{f}{f_y}\right)^n, for f \le f_y \\ \dfrac{f-f_y}{E_{0.2}} + \left(\epsilon_u - \epsilon_{0.2} - \dfrac{f_u - f_y}{E_{0.2}}\right)\left(\dfrac{f-f_y}{f_u-f_y}\right)^m + \varepsilon_{0.2}, for f_y \le f \le f_u \end{cases} \quad (1)$$

Where f and ε are engineering stress and strain, respectively; E is Young's modulus, f_y is the yield (0.2 % proof) stress, f_u is the tensile strength, ε_u and $\varepsilon_{0.2}$ are the strain at f_u and f_y respectively, $E_{0.2}$ is the tangent modulus of the stress-strain curve at the yield strength (0.2 % proof stress), $E_{0.2}$ is defined by Eq. 2; n is the first strain-hardening exponent defining the degree of roundness of the stress-strain curve as defined by Eq. 3. m is the second strain-hardening exponent for the second part of the two-stage model, as defined by Eq. 4.

$$E_{0.2} = E/(1+0{\cdot}002\ n\ (E/f_y)) \quad (2)$$

$$n = \ln(4)/\ln(f_y/\sigma_{0.05}) \quad (3)$$

$$m = 1+3{\cdot}3\ f_y/f_u \quad (4)$$

$\sigma_{0.05}$, in Eq. 3, is the measured 0.05 % proof stress. As presented in Table A 1 of Appendix A, measured mechanical properties of CFS based on the coupon test data by Mishra et al. [13] were employed to derive the CFS material models for each gauge thickness of the studs. Figure A1 in Appendix A shows a great agreement between the predictive true stress-strain curves derived from measured mechanical properties (Table A1) based on [34] and respective true stress-strain curves obtained from the tensile coupon test for selected CFS coupons. A quad linear material model for HRS proposed by Gardner and Yun [35] was adopted to model properties of the HRS grade S235 used at the top and bottom support plates and grade S640 for the M8 bolts. The predictive expressions for describing the material stress-strain behaviour of HRS steel are summarised in *Equation 5*.

$$f(\varepsilon)\begin{cases} = E\varepsilon & \text{for } \varepsilon £ \varepsilon_y \\ = f_y & \text{for } \varepsilon_y £ \varepsilon £ \varepsilon_{sh} \\ = f_y + E_{sh}\left(\varepsilon - \varepsilon_{sh}\right) & \text{for } \varepsilon_{sh} £ \varepsilon £ C1\varepsilon_u \\ = f_{c1\varepsilon u} + (f_u - f_{c1\varepsilon u})/(\varepsilon_u - C1\varepsilon_u) & \text{for } C1\varepsilon_u < \varepsilon < \varepsilon_u \end{cases} \quad (5)$$

In Equation 5, E, f_y, and f_u are Young's modulus, yield stress, and ultimate stress of HRS, respectively. ε_{sh} and E_{sh} are the strain hardening strain and the strain hardening modulus, respectively. C1 is a material coefficient. The values of the key parameter for the standard HRS carbon steel grades employed in this study are derived based on [35]. The engineering stress and strains, calculated based on the original cross-sectional area of coupon specimens, were transformed into true stress and true plastic strains as per [23] for input into the ABAQUS FEA models. The residual stresses and increased yield stress at the corner regions of CFS elements due to cold-working were not modeled as suggested by [30]. The mechanical properties of CFS were assumed to be the same across the cross-section, as other researchers [24,36,37] also followed.

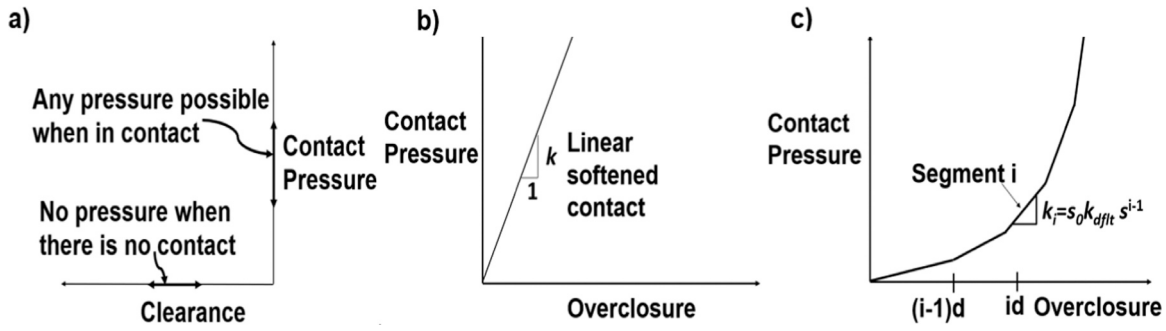

Fig. 6. Pressure-overclosure relationship: a) hard contact (HC), b) linear softened contact (LSC), and c) piecewise linear softened contact (PLSC). Rreproduced from [23].

3.4. Geometric imperfections

The measured geometric imperfections, as reported in Table 1 were incorporated in the FEA models following a method adopted by [36,37]. This consisted of each stud's interactive buckling modes, as was observed during the reference testing program [13], being superimposed during post-buckling analysis to consider the influence of the studs' various imperfection distributions.

3.5. Solver scheme and loading type

A dynamic explicit solver was adopted for the post-buckling analysis with a displacement-controlled loading rate of 1 mm/sec. Mass scaling was employed with the target time increment set to 1e-05 s to improve the computational efficiency further. It was verified that the total kinetic energy of the system was negligible, less than 5–10 % of the internal energy, as recommended in [23], to ensure that the inertia effect is insignificant.

3.6. Contact behaviour

The contact interaction between the stud and tracks along the normal and tangential direction influences the studs' axial compressive stiffness and shortening behaviour post-closure of the stud-to-track gap (i.e., in Phase II). Contact was defined using the general contact algorithm available in ABAQUS/Explicit [23]. A numerical sensitivity study revealed that the contact interaction between the bolts and their surrounding areas did not affect the studs' axial compressive performance other than a nominal (0.2 %) influence in their ultimate capacity; hence, the general contact algorithm was chosen. Moreover, accurately modeling the contact interaction near the tracks' rounded corners was critical to simulate the stud-to-track gap-closing behaviour, which dictated the studs' Phase I axial stiffness, k_1. The general contact algorithm with a 'penalty' constraint enforcement method and mechanical finite-sliding analysis has a unique built-in smoothing feature that is beneficial for modeling such accurate contact interaction near the rounded corner region [23].

3.6.1. Contact normal behaviour

The contact normal behaviour controlled the relative displacements of the studs normal to the track surface. The normal behaviour is defined by various pressure-overclosure relationships, three of which were investigated herein and can be seen in Fig. 6. 1) Hard contact (HC): The HC minimizes the penetration of slave nodes into the master surface and does not allow the transfer of tensile stress across the interface [23]. The contact pressure is either zero when the surfaces are not in contact or 'infinite' when the surfaces come into contact, as shown in Fig. 6a. 2) Linear softened contact (LSC): In a linear softened pressure overclosure relationship (Fig. 6b), the contact stiffness, k, increases linearly as the surfaces come into contact and start deforming due to the transmission of contact pressures between each other. k is generally considered analogous to the linear elastic branch of the bed material's constitutive relation [38].

3) Piecewise linear softened contact (PLSC): The piecewise linear softened pressure overclosure relationship is an improved version of LSC. As shown in Fig. 6c, the default contact stiffness, $k_{dflt,}$ is multiplied by a scaling factor, $s_{0,}$ at the initial loading step. Unlike LSC, in PLSC, the permissible penetration measure, d, is specified by the user. The contact stiffness increases linearly in small segments by multiplying k_{dflt} with another scaling factor s each time the penetration exceeds d during analysis. k_{dflt} is calculated internally in ABAQUS and is the same as the default contact stiffness in HC when s_0 equals 1.

3.6.2. Tangential behaviour

A sensitivity study of the coulomb friction coefficient, μ values ranging between 0.1 and 0.4, revealed no difference in the studs' load axial shortening response other than a nominal (2 %) difference in the peak load. Therefore, a μ value of 0.14 was adopted for all the FEA models in this study as this μ value provided the best agreement with the test results.

4. Validation of the softened contact parameters and test results

The accuracy of the HC, LSC, and PLSC algorithms in predicting the studs' axial compressive behavior with the track-boundary conditions is evaluated herein. Section 4.1 details the initial validation comparison of

Table 3
LSC contact stiffness (k) and PLSC scale factors (s_0, s) for the first stud sample of each cross-section type and height.

Specimen ID	LSC contact stiffness, k (N/mm)	PLSC s	PLSC s_0	Specimen ID	LSC contact stiffness, k (N/mm)	PLSC s	PLSC s_0
S75 −1.2 −1200 −1	1200	1.005	0.0100	S100 −2.0 −1500 −1	1200	1.100	0.0050
S75 −1.2 −1500 −1	1000	1.350	0.0020	S100 −3.0 −1200 −1	1200	1.005	0.0100
S75 −1.5 −1200 −1	1300	1.250	0.0020	S100 −3.0 −1500 −1	1600	1.005	0.0100
S75 −1.5 −1500 −1	1000	2.000	0.0020	S125 −1.3 −1200 −1	650	1.180	0.0015
S100 −1.2 −1200 −1	500	1.010	0.0100	S125 −1.3 −1500 −1	700	1.100	0.0020
S100 −1.2 −1500 −1	600	1.015	0.0100	S125 −2.0 −1200 −1	900	1.100	0.0014
S100 −2.0 −1200 −1	1000	1.050	0.0065	S125 −2.0 −1500 −1	1000	1.012	0.0100

Table 4
Initial validation comparison of studs' Phase I and Phase II axial stiffness (k_1 and k_2) from HC, LSC, and PLSC analysis with test data (on the first stud sample of each cross-section type and height).

Specimen ID	Phase I axial (secant) stiffness, k_1 (kN/mm)		FEA# to test ratio of k_1 (R_{k1}) (HC, LSC & PLSC)	Phase II axial (tangential) stiffness, k_2 (kN/mm)				FEA to test ratio (R_{k2}) of k_2		
	Test	FEA	$R_{k1FEA/test}$	Test	FEA_{HC}	FEA_{LSC}	FEA_{PLSC}	$R_{k2\ HC/test}$	$R_{k2\ LSC/test}$	$R_{k2\ PLSC/test}$
	(1)	(2)	(3)	(4)	(5)	(6)	(7)	(8)	(9)	(10)
S75 −1.2 −1200 −1	3.8	1.2	0.32	5.9	18.03	11.1	11.3	3.06	1.88	1.92
S75 −1.2 −1500 −1	1.5	1.1	0.73	5.3	16.5	9.1	7.9	3.11	1.72	1.49
S75 −1.5 −1200 −1	2.2	2.1	0.95	7.0	31.03	10.8	6.7	4.43	1.54	0.96
S75 −1.5 −1500 −1	2.3	1.3	0.54	5.4	23.9	9.1	5.6	4.43	1.69	1.03
S100 −1.2 −1200 −1	4.6	3.2	0.7	7.4	13.7	8.5	7.6	1.85	1.15	1.03
S100 −1.2 −1500 −1	3.6	1.4	0.39	8.5	12.7	8.9	8.5	1.49	1.05	1.00
S100 −2.0 −1200 −1	5.6	5.1	0.91	11.5	37.4	13.7	13.2	3.25	1.19	1.15
S100 −2.0 −1500 −1	3.4	2.5	0.74	15.0	47.2	17.8	15.1	3.15	1.19	1.01
S100 −3.0 −1200 −1	7.2	3.4	0.47	17.4	58.1	16.5	18.3	3.34	0.95	1.05
S100 −3.0 −1500 −1	3	3.1	1.03	20.2	64.3	20.5	20.5	3.18	1.01	1.01
S125 −1.3 −1200 −1	4.4	4.3	0.98	9.9	26.7	9.7	9.4	2.7	0.98	0.95
S125 −1.3 −1500 −1	3.1	3.2	1.03	9.7	22.2	11.7	9.8	2.29	1.21	1.01
S125 −2.0 −1200 −1	4.5	3.1	0.69	14.7	54.6	13.3	14.8	3.71	0.9	1.01
S125 −2.0 −1500 −1	5.1	2.5	0.49	18.6	37.2	17.6	18.8	2.00	0.95	1.01
Mean			0.70					3.00	1.24	1.12
Standard Deviation			0.24					0.89	0.33	0.27
COV			0.34					0.29	0.26	0.24

k_1 is the same in HC, LSC, and PLSC analyses, with the nonlinear connection stiffness dominating k_1.

the HC, LSC, and PLSC analysis results with test data for the first sample of each stud cross-section with each height. Section 4.2 discusses a complete validation comparison of the numerical FEA model with all forty-two test data by Mishra et al. [13] using the most accurate algorithm determined in Section 4.1.

4.1. Initial validation comparison of the HC, LSC, and PLSC analysis results with test data on the first stud sample of each cross-section and height

Initially, the softened contact parameters are calibrated with test results for the first sample of each stud's cross-section and height and are reported in Table 3. For the LSC analysis, the softened contact stiffness, *k*, was determined based on numerical sensitivity studies, using *k* values as various percentages ranging between 0.25 % to 0.75 % of the bed material's Young's modulus (E = 181365 MPa based on measured mechanical properties for the track sections connected to the studs' at both ends), following a similar methodology adopted by Natario et al. [38] and others [24,25]. The experimental and numerical load-axial shortening responses using various *k* values were compared. The different k values for each stud cross-section and height that provided the best agreement with the test results in terms of studs' Phase II axial stiffness, k_2, peak axial compressive capacity, P_U, and post-peak behavior was selected as the final linear softened contact stiffness, *k*, at the stud-to-track contact interface. Using the PLSC algorithm, a similar method was adopted to that of LSC. In this method, the studs' initial lower nonlinear axial stiffness in Phase II (k_2) was replicated by setting up the initial scaling factor, s_0, as various percentages of the default contact stiffness, k_{dflt} (k_{dflt} is calculated internally in ABAQUS[23], Section 3.6.1) as opposed to the different percentages of the bed material's Young's modulus employed in LSC. The reason for this is that in LSC, the actual value of the softened contact stiffness *k* is required to be provided as an interaction input parameter in ABAQUS [23]. In contrast, in PLSC, the softened contact stiffness scale factors, *s* and s_0, need to be provided. Initially, a low value of s_0, starting from 0.001, meaning 0.1 % of the default contact stiffness, k_{dflt}, was employed for each stud section.

Table 5
Initial validation comparison of axial shortening at peak load, V, and ultimate capacity, P_U, from HC, LSC, and PLSC analysis with test data (on the first stud sample of each cross-section type and height).

Specimen ID	Axial shortening at peak load, V (mm)				FEA to test ratio (R_V) of V			Ultimate capacity, P_u (kN)				FEA to test ratio (R_P) of P_u		
	Test	FEA_{HC}	FEA_{LSC}	FEA_{PLSC}	$R_{V\ HC/test}$	$R_{V\ LSC/test}$	$R_{V\ PLSC/test}$	Test	FEA_{HC}	FEA_{LSC}	FEA_{PLSC}	$R_{PU\ HC/test}$	$R_{PU\ LSC/test}$	$R_{PU\ PLSC/test}$
	(1)	(2)	(3)	(4)	(5)	(6)	(7)	(8)	(9)	(10)	(11)	(12)	(13)	(14)
S75 −1.2 −1200 −1	7.6	6.2	7.4	7.44	0.82	0.97	0.98	33.7	34.2	34.7	31.7	1.01	1.03	0.94
S75 −1.2 −1500 −1	8.4	6.9	8.6	8.03	0.82	1.02	0.96	33.3	36.21	36.8	30.4	1.09	1.11	0.91
S75 −1.5 −1200 −1	11.9	7.2	10.3	11.9	0.61	0.87	1`.00	66.4	72.7	67.9	61.5	1.09	1.02	0.93
S75 −1.5 −1500 −1	13.3	9.9	13.0	13.9	0.74	0.98	1.05	50.8	57.6	48.6	46	1.13	0.96	0.91
S100 −1.2 −1200 −1	8.6	5.4	9.3	7.4	0.63	1.08	0.86	58.9	52.6	49.02	51	0.89	0.83	0.87
S100 −1.2 −1500 −1	9	6.4	8.4	8.3	0.71	0.93	0.92	49.2	53.0	53.2	48.7	1.08	1.08	0.99
S100 −2.0 −1200 −1	10.3	5.7	10.9	10.5	0.55	1.06	1.02	123.1	128.7	121.9	122.5	1.05	0.99	1.00
S100 −2.0 −1500 −1	11.7	7.5	13.3	10.6	0.64	1.14	0.91	125.2	132.8	131.5	123.7	1.06	1.05	0.99
S100 −3.0 −1200 −1	16.6	8.9	16.1	15.1	0.54	0.97	0.91	211.9	226.2	195.7	200.4	1.07	0.92	0.95
S100 −3.0 −1500 −1	12.4	6.6	12.3	12	0.53	0.99	0.97	188.9	211.2	187.9	158.2	1.12	0.99	0.84
S125 −1.3 −1200 −1	6.7	3.3	5.1	6.9	0.49	0.76	1.03	65.3	71.2	59.3	62.9	1.09	0.91	0.96
S125 −1.3 −1500 −1	9.3	4.7	7.7	10.3	0.51	0.83	1.11	65.2	65.8	73.2	65.4	1.01	1.12	1.00
S125 −2.0 −1200 −1	12.6	5.9	12.7	11.9	0.47	1.01	0.94	144.9	145.2	142.2	141.1	1.00	0.98	0.97
S125 −2.0 −1500 −1	11.7	7.8	12.6	11.9	0.67	1.08	1.02	134.9	143.8	125.9	126.4	1.07	0.93	0.94
Mean					0.62	0.98	0.98					1.05	0.99	0.94
Standard Deviation					0.12	0.10	0.07					0.06	0.08	0.05
COV					0.19	0.11	0.07					0.06	0.08	0.05

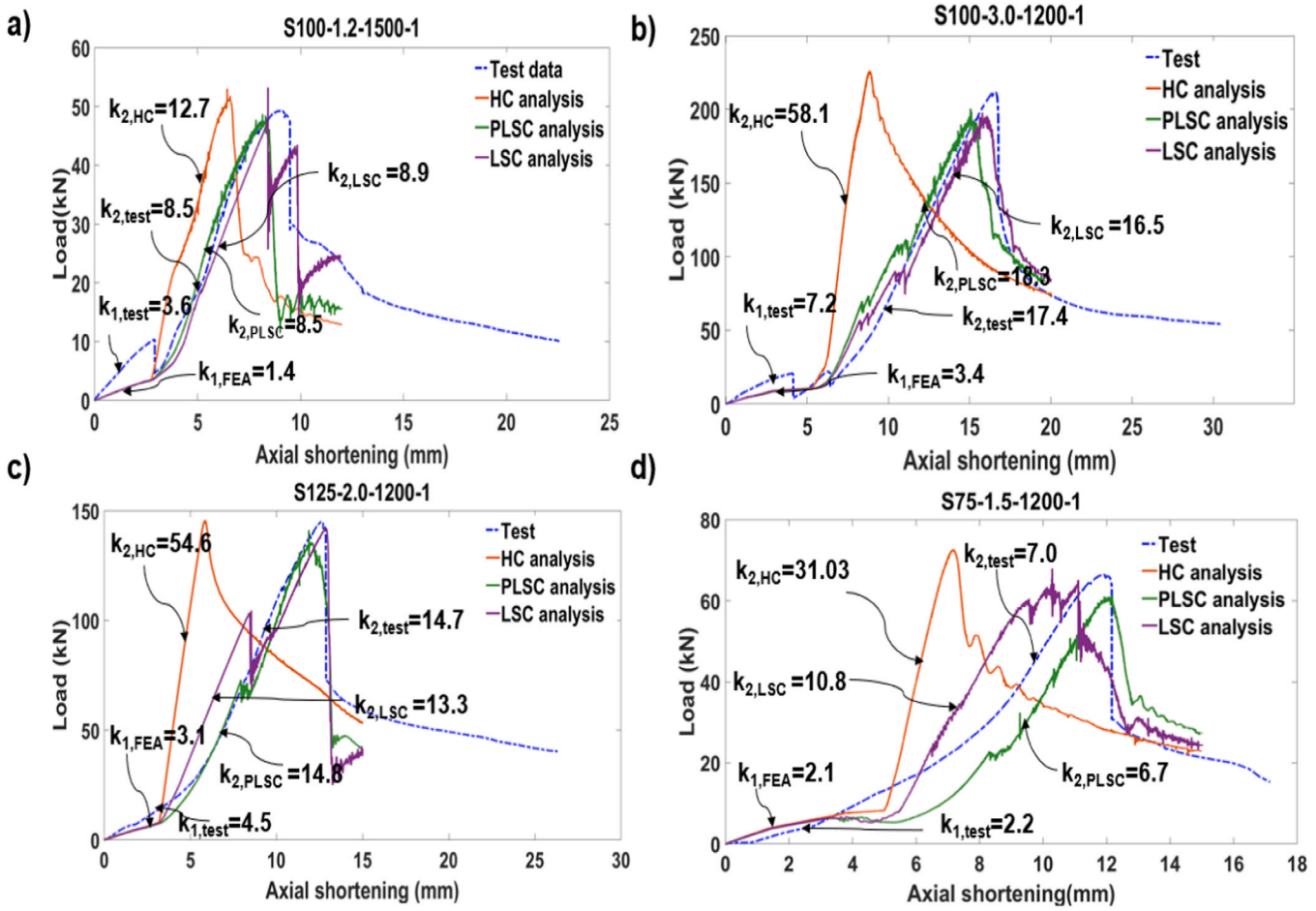

Fig. 7. Initial validation comparison of load vs. axial shortening; analysis vs. test data for HC, LSC, and PLSC: a) S100–1.2-1500–1; b) S100–3.0-1200–1; c) S125–2.0-1200–1; and d) S75–1.5-1200–1.

Based on the ABAQUS documentation [23], the *s* factor should always be greater than 1, since *s* is applied to $s_0 k_{dflt}$ to increase the softened contact stiffness at the stud-to-track interphase each time the penetration exceeds the defined penetration magnitude, *d* during analysis (refer to Fig. 6c). Similar to s_0, a starting value of *s* was employed as a low value, 1.005. The combination of s_0 and *s* scale factors controlled the accuracy of the studs' numerical Phase II axial stiffness, k_2, axial shortening, V, and ultimate axial-compressive capacity, P_U. A numerical sensitivity study was performed with various combinations of *s* and s_0. s_0 varied between 0.1 % to 1 % of k_{dflt}.*s* varied between 1.005 and 2. The most accurate combination of *s* and s_0 values for each stud cross-section type and height was established by comparing the studs' experimental and numerical load axial shortening response. The combination of the *s* and s_0 values, which provided the best agreement with the test data in terms of k_2, P_U, post-peak behaviour, and the failure mechanism, was employed as the final PLSC softened contact parameters at the stud-to-track interface. The measure of the defined penetration *d*, representing the material indentation on the track web, was assumed and assigned to be 0.1 mm (5 % of the track thickness), as the physical indentation on the track web could not be measured due to being very small (refer to Fig. 1d & e).

Table 4, Table 5, and Fig. 7 compare the HC, LSC, and PLSC analysis results with test data for the first stud sample of each stud cross-section type and height. The following key parameters, axial stiffnesses in Phase I & II (k_1 & k_2), axial shortening at ultimate load (V), and the ultimate capacity (P_u), are compared.

In Fig. 7 and Table 4, both the numerical Phase I axial stiffness, k_1, and the Phase II axial stiffness, k_2, are derived from the slope of the trend lines to the numerical load axial shortening curves in Phase I and II, respectively using the HC, LSC, and PLSC algorithms. This method is similar to that adopted by Mishra et al. [13] while deriving the experimental axial stiffness in Phase I and II. The numerical k_1 is a secant stiffness equivalent to the nonlinear connection stiffness, which was incorporated in the FEA models following Pham and Moen's [27] predictive equations. Meanwhile, k_2 is a tangential stiffness, meaning the derivative of nodal force to the nodal displacements in Phase II. The dividing line between the two Phases is visually evident in the experimental and numerical load axial shortening response shown in Fig. 7. Until the stud-to-track gap's closure, the studs exhibit low axial stiffness k_1. The axial stiffness k_2 significantly increases with respect to k_1 once the gap is closed and the stud bears on the track web.

The HC analysis significantly overestimated k_2 by three times (Column 8, Table 4) and underestimated studs' V by 38 % (Column 5, Table 5) compared to the test results. However, HC predicted the studs' P_u reasonably accurately with a 5 % (Column 12, Table 5) overestimation. Others [20] have also highlighted the overestimation of axial lateral stiffness and ultimate capacity using HC. The substantial overestimation of k_2 and underestimation of V is attributed to the sudden rise in the contact pressure to infinity in the HC algorithm (Fig. 6a) when the stud and track contact each other. In reality, the contact pressure increases gradually as the stud and track interact and deform each other due to the transmission of contact pressure at the stud-to-track interface. In addition, the studs' numerical post-peak behaviour with HC did not exhibit the sudden capacity reduction observed during testing (Fig. 7).

Using LSC, an excellent agreement of numerical to test results was

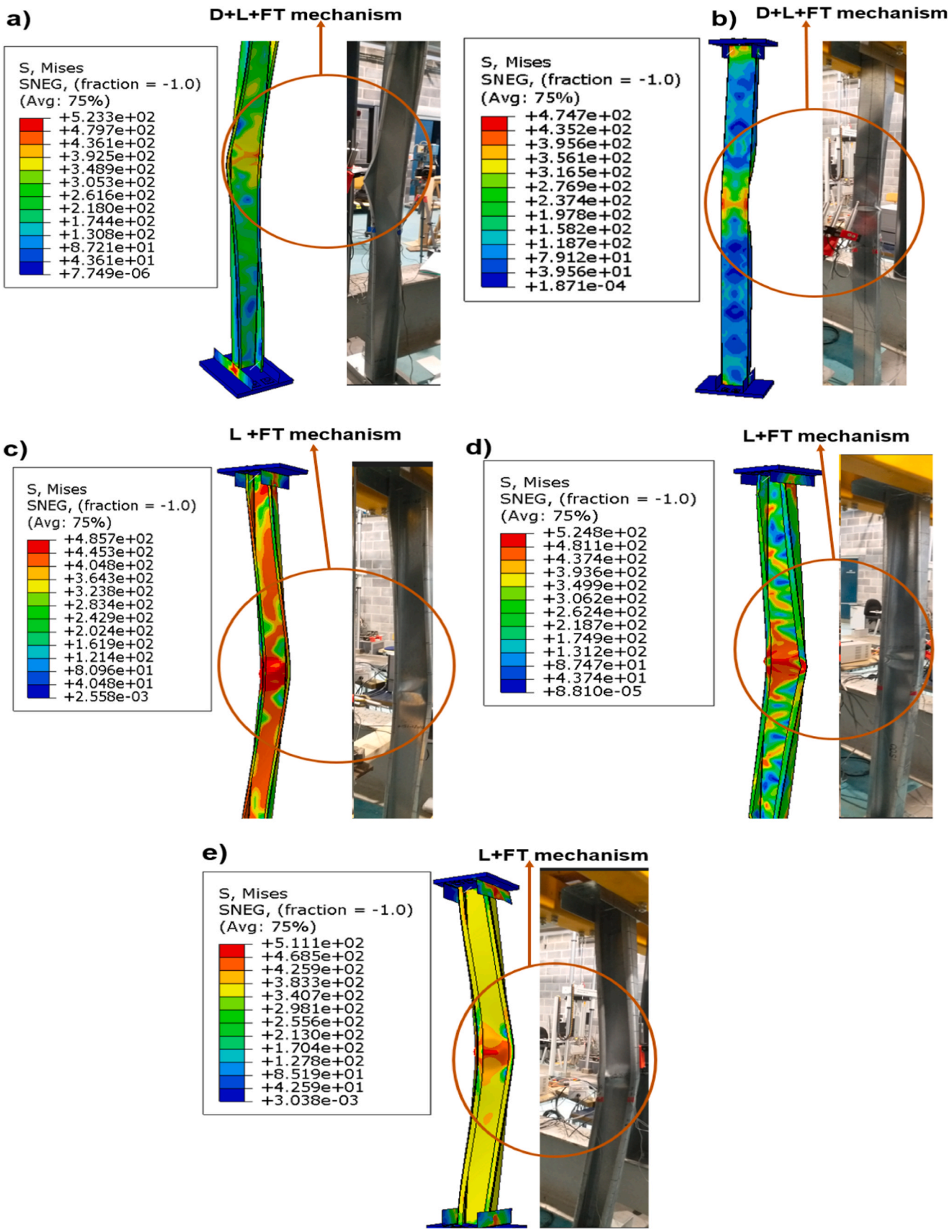

Fig. 8. Test vs. PLSC analysis failure mechanisms: a) S75–1.2-1200–1; b) S100–1.2-1500–1; c) S100–2.0-1500–3; d) S125–1.3-1500–1; e) S100–3.0-1200–1 (D, L, and FT represent distortional, local, and flexural-torsional failure mechanisms).

Table 6
Summary of comparison of FEA_{PLSC} analysis results (key parameters) with all (forty-two) test data.

Specimen ID	Ratio of Phase II axial stiffness, k_2 $R_{k2\ PLSC/test}$			Ratio of axial shortening at peak load, V $R_{V\ PLSC/test}$			Ratio of ultimate capacity $R_{PU\ PLSC/test}$		
(1)	Mean **(2)**	Standard Deviation **(3)**	COV **(4)**	Mean **(5)**	Standard Deviation **(6)**	COV **(7)**	Mean **(8)**	Standard Deviation **(9)**	COV **(10)**
S75 −1.2 −1200	1.80	0.11	0.06	0.95	0.02	0.02	0.94	0.02	0.02
S75 −1.2 −1500	1.51	0.02	0.01	0.96	0.05	0.05	0.91	0.02	0.02
S75 −1.5 −1200	1.02	0.08	0.08	0.90	0.14	0.16	0.91	0.03	0.03
S75 −1.5 −1500	1.00	0.05	0.05	1.00	0.07	0.07	0.87	0.06	0.07
S100 −1.2 −1200	1.00	0.05	0.05	0.88	0.03	0.03	0.85	0.03	0.04
S100 −1.2 −1500	1.00	0.01	0.01	0.95	0.04	0.04	0.93	0.05	0.05
S100 −2.0 −1200	1.06	0.08	0.08	1.02	0.01	0.01	0.98	0.02	0.02
S100 −2.0 −1500	1.00	0.01	0.01	0.99	0.07	0.07	0.96	0.02	0.02
S100 −3.0 −1200	1.04	0.02	0.02	0.89	0.03	0.03	0.96	0.03	0.03
S100 −3.0 −1500	1.00	0.01	0.01	0.93	0.05	0.05	0.88	0.06	0.07
S125 −1.3 −1200	0.98	0.07	0.07	1.03	0.00	0.00	0.98	0.04	0.04
S125 −1.3 −1500	0.95	0.10	0.11	1.04	0.18	0.17	1.02	0.02	0.02
S125 −2.0 −1200	1.00	0.01	0.01	0.99	0.05	0.05	0.99	0.02	0.02
S125 −2.0 −1500	1.02	0.02	0.02	1.03	0.01	0.01	0.96	0.02	0.02
Overall Average	1.01#	0.05	0.04	0.97	0.05	0.05	0.94	0.03	0.03

Overall average of $R_{k2\ PLSC/test}$ excluding the S75-1.2 studs.
The overall average of $Rk_{2\ PLSC/test}$ for all studs, including the S75-1.2 studs is 1.10.

obtained only for the thickest 3 mm gauge studs (Fig. 7b). Overall, the studs' numerical k_2 was overestimated by 24 % (Column 9, Table 4), while V (Column 6, Table 5) and P_u (Column 13, Table 5) magnitudes were underestimated by 2 % and 1 %, respectively. However, for the 2 mm and 1.5 mm gauge studs, significant noise was observed in the numerical load-axial shortening response close to the peak load (Fig. 7a, c,d). Additionally, for the thinner gauge (1.2 mm & 1.25 mm) studs, excessive deformation of the stud section occurred near the track web in the FEA. This behaviour is attributed to the contact stiffness, *k*, increasing at a constant rate (linearly) throughout the LSC analysis (Fig. 6b), which did not restrict the penetration enough, causing the substantial numerical deformation of the thinner gauge (<3 mm) studs' web. Consequently, the numerical failure mechanism using LSC did not match the test results [13].

Using the PLSC algorithm, on average, the studs' k_2 (Column 10, Table 4) was slightly overestimated by 1 % for all studs except for the S75–1.2 studs. On average, V (Column 7, Table 5) and P_U (Column 14, Table 5) were underestimated by 2 % and 6 %, respectively. The studs' post-peak sudden capacity reduction (Fig. 7) and failure mechanisms were captured accurately using PLSC. The accuracy of PLSC is because, unlike HC, in PLSC, the stud web was allowed to penetrate the track web numerically but with a restricted magnitude *d* (specified as 0.1 mm), representing the indentation on the track web observed in reality during testing [13]. In addition, the scale factor, *s*, increased the contact stiffness whenever the stud penetrated the track more than the specified *d* during analysis. Compared to HC and LSC, the PLSC analysis most accurately replicated the studs' axial stiffness (k_2), shortening (V), ultimate axial compressive capacity (P_U), failure mechanism, and post-peak response. Fig. 8 compares the visual observation of the studs' failure mechanism due to complex buckling mode interaction at peak load in the test versus PLSC analysis for selected studs, which also agrees well.

During loading Phase I, until the stud-to-track gap was closed, the stud and track webs did not come into contact. Hence, the stud-to-track contact behaviour along the normal direction did not affect the studs' Phase I axial stiffness k_1; instead, the nonlinear connection stiffness dominated it. Thus, k_1 was the same in the HC, LSC, and PLSC analyses and was underestimated by 30 % in FEA (Column 3, Table 4).

4.2. Complete validation comparison of the accuracy and repeatability of the established PLSC scale factors, s_0 and s, with all (forty-two) test data

As the PLSC was observed to be the most accurate contact-modeling approach, the validity of the initially verified PLSC scale factors, s_0 and *s* magnitudes, established in Section 4.1, is investigated herein thoroughly with all forty-two tested stud samples used in the detailed experimental testing by Mishra et al. [13].

The scale factors for the first sample of each stud cross-section type were applied over the second and third samples. All studs' and tracks' measured geometries [13] and other measured parameters for each stud and track were used from Table 1. A summary of the detailed analysis results using PLSC on all the tested forty-two studs, comparing all the key parameters k_2, V, and P_u, with test data are reported in Table 6. Overall, the studs' k_2 (Column 2, Table 6) was overestimated by 1 %, excluding the S75–1.2 studs. Only for the S75–1.2 studs the analytical k_2 was higher than the experimental one, as shown in (Column 2, Table 6). The V (Column 5, Table 6) and P_u (Column 8, Table 6) of all the studs were underestimated by 3 % and 6 %, respectively.Fig. 9 and Fig. 10 show the repeatability of selected studs' experimental and numerical load versus axial shortening response using the PLSC analysis and their comparison with all test results. It can be observed that both pre-peak and post-peak behaviour was predicted accurately for every sample.

5. Novel predictive equations to determine PLSC scale factors

The PLSC scale factors, s_0 and *s*, established in this study were found to be closely related to the studs' nondimensional slenderness, λ, calculated as per EC3 [14]. It was investigated and revealed that *s* and s_0 did not follow any correlation with the track-to-stud thickness ratios and material properties such as the Youngs' modulus of CFS. The authors' reference testing program [13] suggested an effective length factor, E_L of 0.65, that considers the warping rigidity provided by the track boundary condition to predict the studs' optimal and safe axial compressive capacity. This section proposes novel predictive equations between the PLSC scale factors s_0, *s*, and the studs' nondimensional slenderness, $\lambda_{0.65\ L}$ corresponding to the E_L of 0.65. Table 7 shows the average $\lambda_{0.65\ L}$ for each stud cross-section type and their respective validated s_0 and *s* factors. Fig. 11 exhibits two novel bilinear relationships: a) between the studs' $\lambda_{0.65\ L}$ and *s*, and b) between *s* and s_0. It can be observed from Fig. 11 a that for $\lambda_{0.65\ L}$ magnitude between 0.49 to 0.95, the *s* value is almost constant, between 1.005 to 1.18 (also reported in Table 7). For

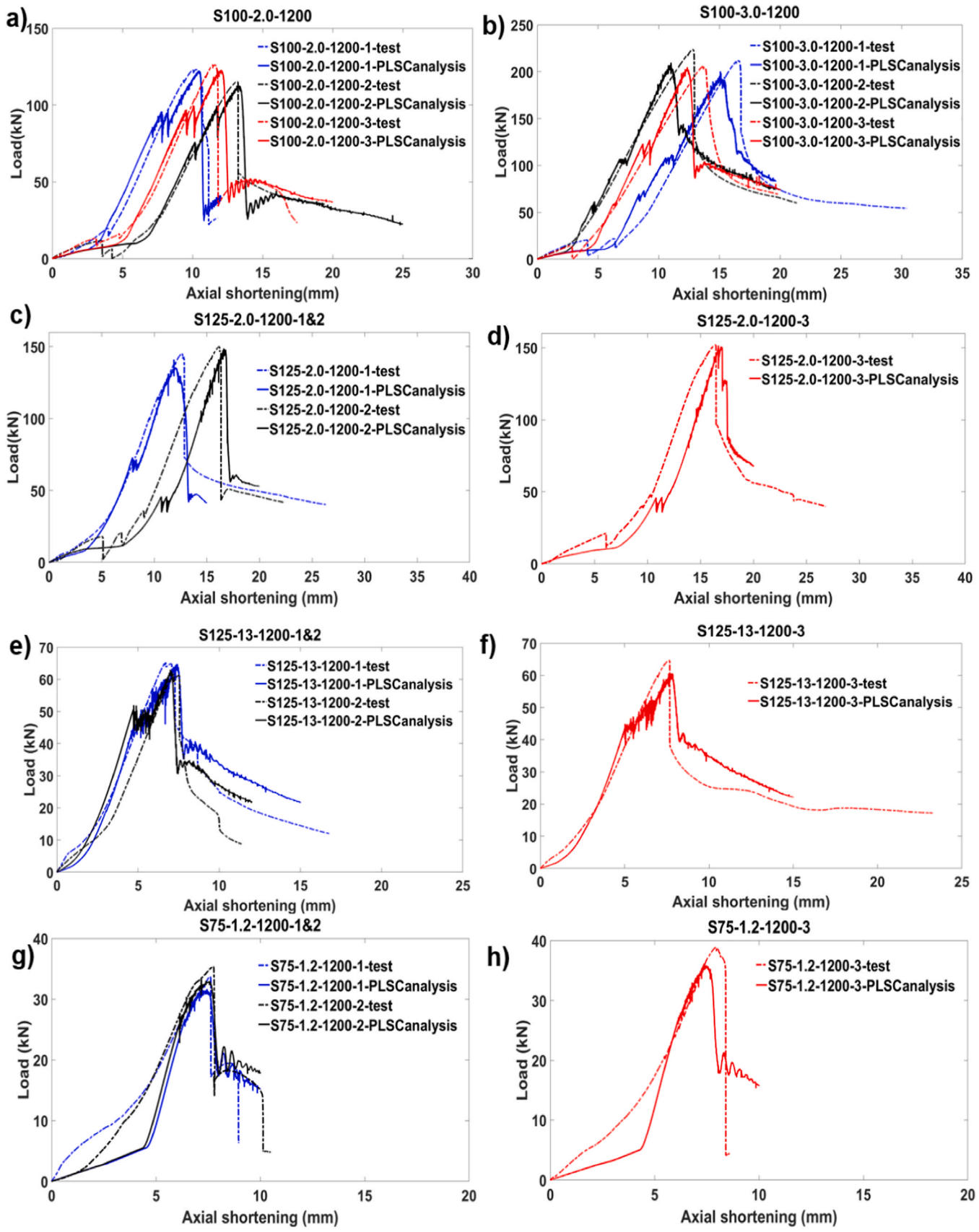

Fig. 9. Load vs. axial shortening in PLSC vs. all test data: a) S100–2.0-1200; b) S100–3.0-1200; c) S125–2.0-1200–1&2; d) S125–2.0-1200–3; e) S125–1.3-1200–1&2; f) S125–1.3-1200–3; g) S75–1.2-1200–1&2; h) S75–1.2-1200–3.

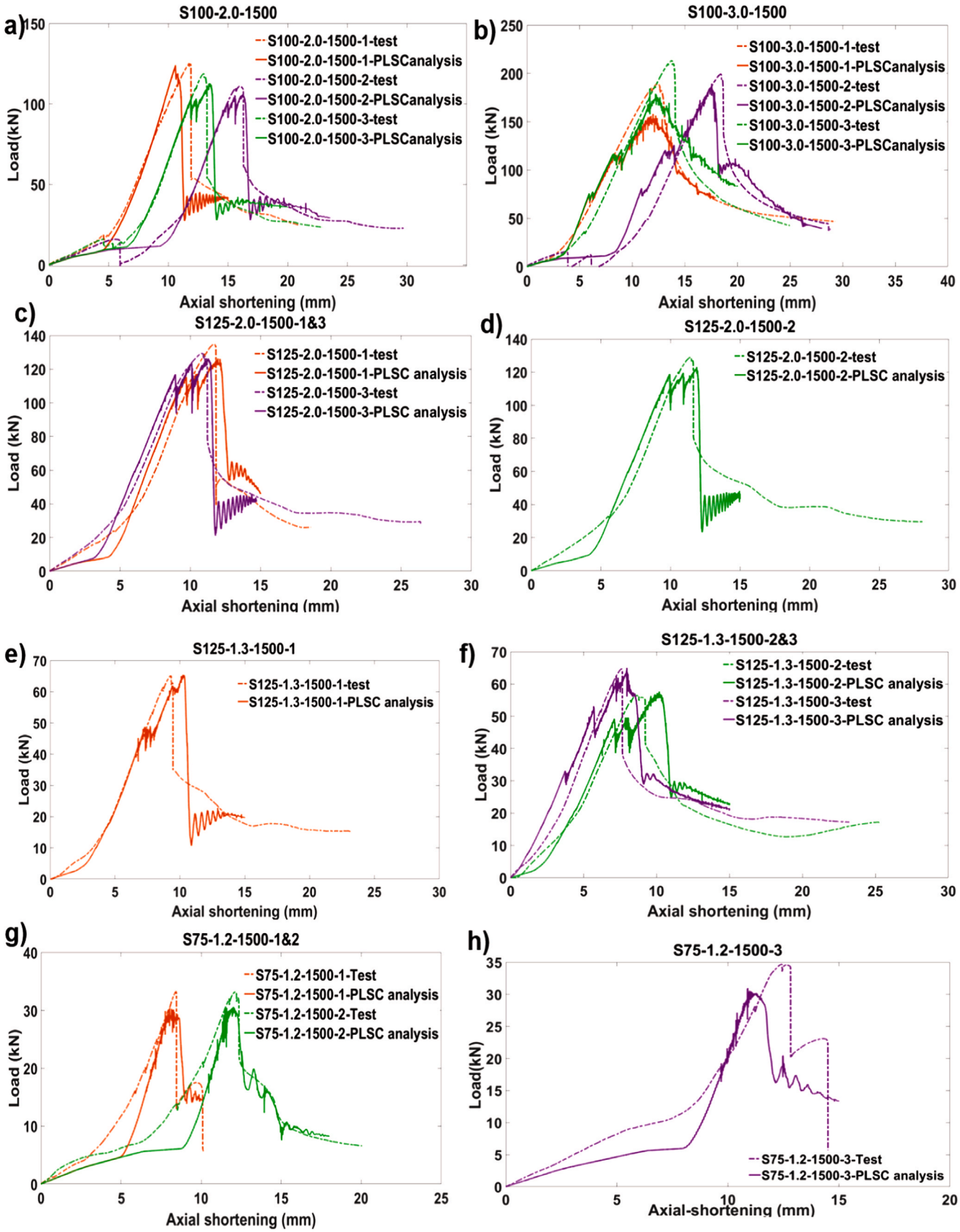

Fig. 10. Load vs. axial shortening in PLSC vs all test data: a) S100–2.0-1500; b) S100–3.0-1500; c) S125–2.0-1500–1&3; d) S125–2.0-1500–2; e) S125–1.3-1500–1; f) S125–1.3-1500–2&3; g) S75–1.2-1500–1&2; g) S75–1.2-1500–3;.

Table 7
Nondimensional slenderness versus PLSC softened contact scale factors.

Specimen ID	Average, $\lambda_{0.65L}$	s	s_0	Specimen ID	Average, $\lambda_{0.65L}$	s	s_0
S75 −1.2 −1200	0.9000	1.005	0.0100	S100 −2.0 −1500	1.0000	1.100	0.0050
S75 −1.2 −1500	1.0900	1.350	0.0020	S100 −3.0 −1200	0.7300	1.005	0.0100
S75 −1.5 −1200	0.9900	1.250	0.0020	S100 −3.0 −1500	0.8800	1.005	0.0100
S75 −1.5 −1500	1.2000	2.000	0.0020	S125 −1.3 −1200	0.5000	1.180	0.0015
S100 −1.2 −1200	0.6400	1.010	0.0100	S125 −1.3 −1500	0.4900	1.100	0.0020
S100 −1.2 −1500	0.7900	1.015	0.0100	S125 −2.0 −1200	0.5300	1.100	0.0014
S100 −2.0 −1200	0.8100	1.050	0.0065	S125 −2.0 −1500	0.6500	1.012	0.0100

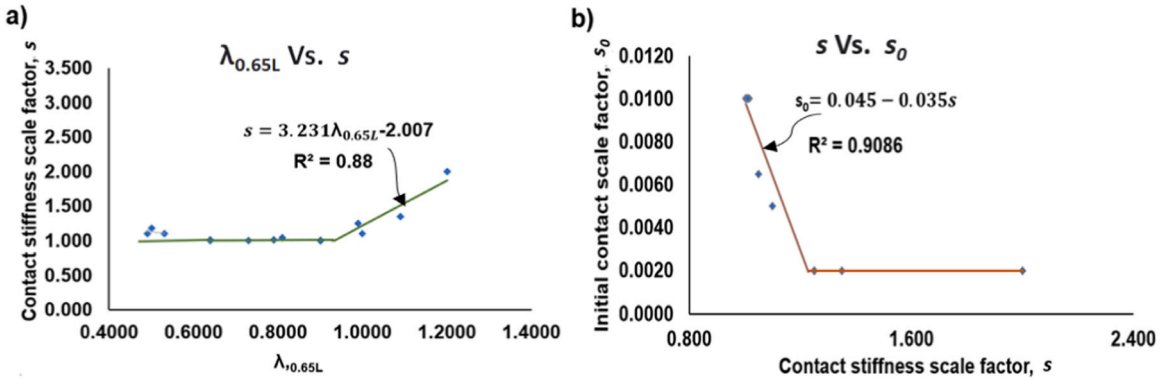

Fig. 11. Generalised softened contact scale factors relationship: a) $\lambda_{,0.65\,L}$ vs. s; and b) s vs s_0.

the $\lambda_{0.65\,L}$ magnitude greater than 0.95, the s value follows a linearly increasing relationship with $\lambda_{0.65\,L}$. This behaviour signifies that the studs with higher non-dimensional slenderness ($\lambda_{0.65\,L} > 0.95$) tend to deform more than studs with lower $\lambda_{0.65\,L}$ (< 0.95) at both stud end portions in contact with the track while penetrating the track web due to the transfer of contact pressure at the stud-to-track interface. The increased contact stiffness (s x k_{dflt}) in PLSC restricts the studs' deformation and penetration into the track web beyond d. Thus, to restrict unwarranted penetration of the stud into the track, the scale factor s is higher for studs having higher slenderness, $\lambda_{0.65\,L} > 0.95$, than those with $\lambda_{0.65\,L} < 0.95$. Based on this study, as shown in Fig. 11 a), s follows a linearly increasing relationship with $\lambda_{0.65\,L}$, which can be expressed by Eq. 1b, for $\lambda_{0.65\,L}$ ranging between 0.95 and 1.2. For $\lambda_{0.65\,L}$ between 0.49 and less than 0.95, s is considered 1.005, a constant value as per Fig. 11 a, as shown in Eq. 6a.

$$s = 1{\cdot}005 \text{ for, } 0{\cdot}49 \leq \lambda_{0{\cdot}65\,L} < 0{\cdot}95 \tag{6a}$$

$$s = 3{\cdot}231\ \lambda_{0{\cdot}65\,L} - 2{\cdot}007 \text{ for, } 0{\cdot}95 \leq \lambda_{0{\cdot}65\,L} \leq 1{\cdot}2 \tag{6b}$$

Fig. 11 b shows that, for the magnitude of s between 1.005 and 1.25, s_0 decreased from 0.01 to 0.002 following a linear relationship (also shown in Equation 7a). This behaviour can be explained as a lower scale factor, s, requiring a higher initial stiffness factor, s_0, to restrict the penetration (and vice-versa). For an s value greater than 1.25, the required s_0 was constant with a magnitude of 0.002, as shown in Equation 7b.

$$s_0 = 0{\cdot}045 - 0{\cdot}035\ s \text{ for, } 1{\cdot}005 \leq s < 1{\cdot}25 \tag{7a}$$

$$s_0 = 0{\cdot}002 \text{ for, } s \geq 1{\cdot}25 \tag{7b}$$

6. Conclusions

A new and accurate FEA contact modeling approach to predict the axial compressive behaviour of bare CFS-lipped channel sections (studs) under concentric axial-compressive static loading with semirigid track boundary conditions has been developed in this study. The ranges of stud cross-sections investigated in this study are the most commonly used in the industry for the CFS wall panels, with panel heights ranging from 2.4 m to 3 m, with noggings/blockings to provide lateral restraint about the studs' minor axis at mid-height. Currently, studs in CFS wall panels are generally designed considering ideal pinned boundary conditions and not track boundary conditions with semi-rigidity, primarily due to simplicity, test results, and numerical modeling approaches not being available for the track boundary conditions. The authors' recent test results [13] on forty-two industry standards bare CFS studs under axial compressive loading with track boundary conditions are used to validate the FEA models.

For the first time, for axially loaded bare CFS studs, softened contact algorithms are investigated with a) linear (LSC) and b) piecewise linear (PLSC) pressure overclosure relations to simulate the stud-to-track contact behaviour in the normal direction. The LSC contact stiffness (k) and the PLSC scale factors (s_0, s) were established through detailed numerical analysis and validation with the test data. The softened contact analysis results are compared with hard contact (HC), which is widely used in literature due to its simplicity. In the tangential direction, the penalty friction with a Coulomb's friction coefficient of 0.14 is used in all three (HC, LSC, and PLSC) analysis types. The results of the comparative study between HC, LSC, and PLSC are summarised below:

- Compared to the test results, the HC analysis substantially overestimated the studs' axial stiffness, three times more and underestimated axial shortening by 38 %. The HC did not capture the studs' post-peak sudden capacity reduction. However, it reasonably predicted the studs' ultimate axial-compressive capacity with a 5 % overestimation.
- The LSC analysis did not predict the accurate failure mechanism of the studs thinner than 3 mm gauge thickness, which resulted in significant noise in the load-axial shortening response near the peak load.
- The PLSC analysis, with the validated scale factors s_0 and s, established in this study, most accurately replicated all the studs' axial compressive behaviour, including the stud-to-track gap closure and

precise two-phased axial stiffness. The axial stiffness post-gap closure was slightly overestimated by 1 %, while the axial shortening and ultimate axial-compressive capacity were underestimated by 3 % and 6 %, respectively. In addition, the PLSC analysis precisely replicated the studs' sudden post-peak capacity reduction and the complex buckling mode interaction at failure, as observed during testing.

The PLSC scale factors, s_0 and s, were found to be closely correlated with the studs' nondimensional slenderness ($\lambda_{0.65\,L}$) following a bi-linear relation. Novel predictive equations were developed to determine accurate s_0 and s, within the practical ranges of $\lambda_{0.65\,L}$, between 0.49 and 1.2 of the industry standard studs used in CFS wall panels. The new predictive equations will enable designers to use accurately calibrated models to capture bare studs' complex axial compressive behaviour in the elastic and inelastic range.

CRediT authorship contribution statement

Sohini Mishra: Writing – review & editing, Writing – original draft, Visualization, Validation, Software, Resources, Project administration, Methodology, Investigation, Formal analysis, Data curation, Conceptualization. **Daniel P. McCrum:** Writing – review & editing, Supervision, Resources, Project administration, Funding acquisition, Conceptualization.

Declaration of Competing Interest

The authors declare that they have no known competing financial interests or personal relationships that could have appeared to influence the work reported in this paper.

Data Availability

Research data is provided within the manuscript.

Acknowledgment

This research is funded by a School of Civil Engineering, University College Dublin Ph.D. Scholarship. The authors wish to acknowledge the Irish Centre for High-End Computing (ICHEC) for providing computational facilities and support and BW Industries for providing the test specimens free of charge.

Appendix A

Table A1
Measured average mechanical properties of flat coupons from tensile test [13].

Coupon thickness (including galvanization)	Base metal thickness	Young's Modulus, E	Proof strength, $\sigma_{0.2\%}$	Ultimate strength, σ_u	strain at σ_u, ε_u	Grade of steel as per BS EN 10346:2015, Table 8[39]	Nominal proof strength, Rp_{02}[39]	Nominal ultimate strength, R_m[39]
(mm)	(mm)	(MPa)	(MPa)	(MPa)	(%)	(MPa)	(MPa)	(MPa)
3.0	3.00	210340.8	382.3	511.1	13	S350GD	350	420
2.0	1.98	181365	439.7	486.6	8	S420GD	420	480
1.5	1.46	216370.5	518.9	575.4	11	S450GD	450	510
1.25	1.22	210598.8	458.6	526.9	16	S450GD	450	510
1.2	1.18	179223.7	366.2	474.9	16	S350GD	350	420

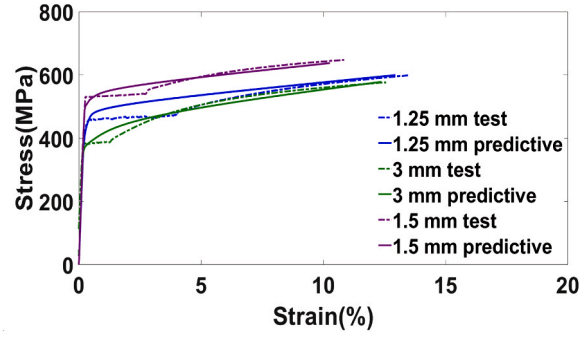

Fig. A1. True stress-strain curves derived from measured mechanical properties as per [34] for selected CFS flat coupons.

.

References

[1] Davies J. Recent research advances in cold-formed steel structures. J Constr Steel Res 2000;55:267–88.
[2] Lim J, Nethercot D. Design and development of a general cold-formed steel portal framing system. Struct Eng 2002;80:31–9.
[3] Schafer BW. Cold-formed steel structures around the world. Steel Constr 2011;4:141–9.

[4] Dubina D., Ungureanu V., Landolfo R. Design of cold-formed steel structures, Eurocode 3: Design of Steel Structures Part 1–3: ECCS – European Convention for Constructional Steelwork; 2012.
[5] SCI P262: Durability of Light Steel Framing in Residential Building, United Kingdom, 2009.
[6] SCI P328: Case Studies on Residential Buildings using Steel, United Kingdom, 2003.
[7] NAHB Research Center I. Galvanized Steel Framing for Residential Buildings. American Iron and Steel Institute; 2007.
[8] Kechidi S, Fratamico DC, Schafer BW, Castro JM, Bourahla N. Simulation of screw connected built-up cold-formed steel back-to-back lipped channels under axial compression. Eng Struct 2020;206:110109.
[9] Kyvelou P, Kyprianou C, Gardner L, Nethercot D. Challenges and solutions associated with the simulation and design of cold-formed steel structural systems. Thin-Walled Struct 2019;141:526–39.
[10] Papargyriou I, Hajirasouliha I, Becque J, Pilakoutas K. Performance-based assessment of CFS strap-braced stud walls under seismic loading. J Constr Steel Res 2021;183:106731.
[11] Gunalan S, Mahendran M. Improved design rules for fixed ended cold-formed steel columns subject to flexural–torsional buckling. Thin-Walled Struct 2013;73:1–17.
[12] LaBoube RA, Findlay PF. Wall stud-to-track gap: experimental investigation. J Archit Eng 2007;13:105–10.
[13] Mishra S, McCrum DP, McNally C, Wrzesien A. Experimental axial-compressive behaviour of bare cold-formed-steel studs with semirigid-track and ideal-hinged boundary-conditions. Published online DOI: https://doiorg/101016/jjcsr2024108600 J Constr Steel Res 2024. Published online DOI: https://doiorg/101016/jjcsr2024108600.
[14] CEN, EN1993–1-3 Eurocode 3: Design of steel structures, Part 1.3: Supplementary Rules for Cold-Formed Members and Sheeting. European Committee for Standardization, Brussels, 2006.
[15] Lawson RM, Way AGJ, Heywood M, Lim JBP, Johnston R, Roy K. Stability of light steel walls in compression with plasterboards on one or both sides. Proc Inst Civ Eng - Struct Build 2020;173:394–412.
[16] Vieira LCM, Shifferaw Y, Schafer BW. Experiments on sheathed cold-formed steel studs in compression. J Constr Steel Res 2011;67:1554–66.
[17] Ye J, Feng R, Chen W, Liu W. Behavior of cold-formed steel wall stud with sheathing subjected to compression. J Constr Steel Res 2016;116:79–91.
[18] Wu H, Chao S, Zhou T, Liu Y. Cold-formed steel framing walls with infilled lightweight FGD gypsum Part II: Axial compression tests. Thin-Walled Struct 2018;132:771–82.
[19] Sonkar C, McCrum DP. Axial compressive behaviour of cold-formed steel single-stud wall panels with one-sided sheathing and two-sided dissimilar sheathing board configurations: experimental and analytical study. Thin-Walled Struct 2023;187:110733.
[20] Niari SE, Rafezy B, Abedi K. Seismic behavior of steel sheathed cold-formed steel shear wall: experimental investigation and numerical modeling. Thin-Walled Struct 2015;96:337–47.
[21] Kyprianou C, Kyvelou P, Gardner L, Nethercot DA. Finite element modelling of sheathed cold-formed steel beam–columns. Thin-Walled Struct 2023;183:110365.
[22] Papargyriou I, Hajirasouliha I. More efficient design of CFS strap-braced frames under vertical and seismic loading. J Constr Steel Res 2021;185:106886.
[23] Dassault Systemes, Abaqus 6.14 Analysis User's Guide: Analysis II, Vol. 142014.
[24] Natário P, Silvestre N, Camotim D. Web crippling failure using quasi-static FE models. Thin-Walled Struct 2014;84:34–49.
[25] Janarthanan B, Mahendran M, Gunalan S. Numerical modelling of web crippling failures in cold-formed steel unlipped channel sections. J Constr Steel Res 2019;158:486–501.
[26] Sundararajah L, Mahendran M, Keerthan P. Experimental studies of lipped channel beams subject to web crippling under two-flange load cases. J Struct Eng 2016;142.
[27] Pham H.S., Moen C.D. Stiffness and strength of single shear cold-formed steel screw-fastened connections. 2015.
[28] Ye J, Mojtabaei SM, Hajirasouliha I. Local-flexural interactive buckling of standard and optimised cold-formed steel columns. J Constr Steel Res 2018;144:106–18.
[29] Ye J, Quan G, Kyvelou P, Teh L, Gardner L. A practical numerical model for thin-walled steel connections and built-up members. Structures 2022;38:753–64.
[30] Schafer BW, Li Z, Moen CD. Computational modeling of cold-formed steel. Thin-walled Struct 2010;48:752–62.
[31] Gardner L. Stability and design of stainless steel structures–Review and outlook. Thin-Walled Struct 2019;141:208–16.
[32] Walport F, Gardner L, Real E, Arrayago I, Nethercot DA. Effects of material nonlinearity on the global analysis and stability of stainless steel frames. J Constr Steel Res 2019;152:173–82.
[33] Ramberg W., Osgood W. Determination of stress-strain curves by three parameters. NACA Technical Note. 1941.
[34] Gardner L, Yun X. Description of stress-strain curves for cold-formed steels. Constr Build Mater 2018;189:527–38.
[35] Yun X, Gardner L. Stress-strain curves for hot-rolled steels. J Constr Steel Res 2017;133:36–46.
[36] Chen B, Roy K, Fang Z, Uzzaman A, Raftery G, Lim JB. Moment capacity of back-to-back cold-formed steel channels with edge-stiffened holes, un-stiffened holes, and plain webs. Eng Struct 2021;235:112042.
[37] Roy K, Chen B, Fang Z, Uzzaman A, Chen X, Lim JB. Local and distortional buckling behaviour of back-to-back built-up aluminium alloy channel section columns. Thin-Walled Struct 2021;163:107713.
[38] Natario P, Silvestre N, Camotim D. Computational modelling of flange crushing in cold-formed steel sections. Thin-Walled Struct 2014;84:393–405.
[39] BS EN 10346. Continuously hot-dip coated steel flat products for cold forming — Technical delivery conditions. 2015.